Research Article

Photoluminescence of CdSe Nanowires Grown With and Without Metal Catalyst

Andrea Fasoli[1], Alan Colli[2], Faustino Martelli[3], Simone Pisana[1], Ping Heng Tan[4], and Andrea C. Ferrari[1] (✉)

[1] Department of Engineering, University of Cambridge, Cambridge CB3 0FA, UK

[2] Nokia Research Centre, Broers Building (East Forum), Cambridge CB3 0GT, UK

[3] Istituto per la Microelettronica e i Microsistemi del CNR, 00133 Rome, Italy

[4] SKLSM, Institute of Semiconductors, Chinese Academy of Sciences, Beijing 100083, China

ABSTRACT

We present temperature and power dependent photoluminescence measurements on CdSe nanowires synthesized via vapor-phase with and without the use of a metal catalyst. Nanowires produced without a catalyst can be optimized to yield higher quantum efficiency, and narrower and spatially uniform emission, when compared to the catalyst-assisted ones. Emission at energies lower than the band-edge is also found in both cases. By combining spatially-resolved photoluminescence and electron microscopy on the same nanowires, we show that catalyst-free nanowires exhibit a low-energy peak with sharp phonon replica, whereas for catalyst-assisted nanowires low-energy emission is linked to the presence of nanostructures with extended morphological defects.

KEYWORDS

CdSe, nanowires, photoluminescence

1. Introduction

Direct band-gap semiconductor nanowires (NWs) have great potential for nano-photonic devices [1–3], including solar cells [4, 5], light emitting diodes [6], and photodetectors [7]. CdSe is particularly interesting for photovoltaics [4, 8], since its band-gap [9] favors absorption over a wide range of the visible spectrum. The preparation of CdSe nanocrystals has been intensively investigated: solution- [10] or vapor-phase processes [11] give a variety of shapes, ranging from NWs to tetrapods or nanosaws [10–14].

Photoluminescence (PL) is an established technique to gain insights on the optical quality of semiconductors. For direct band-gap NWs, PL is often measured over large ensembles [15–22]. This, however, can hinder the extrapolation of representative features as structural inhomogeneities may be present. There have been a number of investigations of PL emission from individual II–IV NWs, mostly at room-temperature (*RT*) [7, 23–28]. However, many radiative states have a binding energy lower than *RT*, and thus cannot be seen [7]. Low-temperature PL of individual II–IV NWs was recently reported [29]. However, understanding the origin of intra band-gap states also requires investigating the dependence of PL emission on power, as was done for NWs in Refs. [17, 28, 30–32].

Address correspondence to acf26@eng.cam.ac.uk

Springer

NWs can be synthesized through a metal catalyst-assisted process [33], with the metal particle being either liquid [33–36] or solid [37–41]. However, impurities such as Au [15, 42–44], Ag [16], or Ni [22] could potentially be incorporated in the growing NW. Therefore, catalyst-free NW growth is being pursued to avoid such contamination, and has been demonstrated for Si [45, 46], Ge [45], InAs [47], GaN [48], InP [49], ZnO [50], and CdSe [51] NWs. The catalyst-free growth of II–IV NWs with a wurtzite structure [50, 51] is driven by the difference in surface energy along specific crystallographic directions [52].

Here, we present temperature and power dependent micro-PL measurements on individual CdSe NWs synthesized via vapor-phase with and without a metal catalyst. We find that NWs grown from Au seeds have broad emission, due to recombinations via intra-band-gap levels. On the other hand, NWs grown without a metal seed have PL features closely resembling those of crystalline bulk CdSe. By coupling spatially-resolved single-NW PL and transmission electron microscopy (TEM), we identify recombinations that are intrinsic for all NWs, as well as extrinsic recombinations due to morphological defects. We assign the difference in optical emission between catalyst-assisted and catalyst-free NWs to the differences in structural quality. NWs produced without a metal catalyst can be optimized to yield higher PL quantum efficiency, narrower emission peaks and better uniformity over large areas, while the catalyst-assisted process has a greater tendency to give rise to structural and optical in-homogeneities.

2. Photoluminescence of bulk CdSe

Before considering PL from CdSe NWs, it is important to analyze the PL features in bulk and thin film CdSe [9, 53–60]. An unambiguous match between emission peaks (or bands) measured by different groups is difficult, and a full understanding of the origin of each band is still missing. The position and width of several PL features can change for different temperature [53, 55], stress [53] or sample contamination [58, 61].

Table 1 summarizes the main PL features for bulk CdSe, as reported in Refs. [9, 53–60]. We classify the bands in various families, according to peak position, lineshape, or suggested literature assignment. We

graphically summarize the content of Table 1 in Figs. 1(a) and 1(b). The PL peaks are marked with symbols, their abscissa indicating the energy (linear scale), and the ordinate the measurement temperature (logarithmic scale). The temperature dependence of the bulk CdSe band-gap is also shown (black line) [62]. Figs. 1(a) and 1(b) associate with every symbol a schematic line-shape, to indicate the width as reported in the literature, as well as possible phonon replicas or overlapping peaks. The intensity is arbitrary.
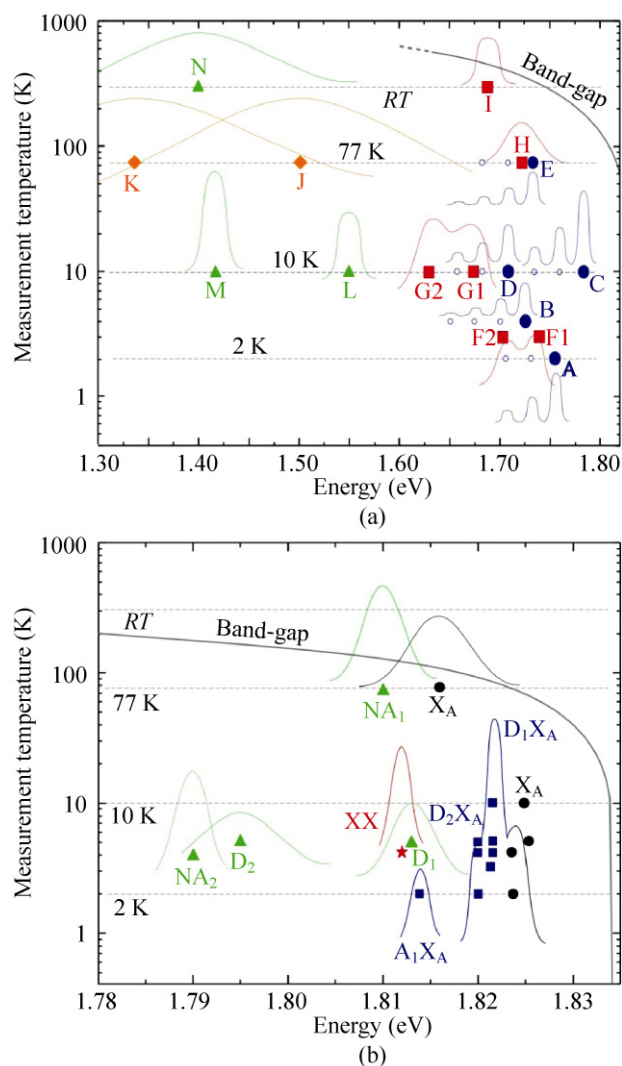

Figure 1 PL contributions reviewed in Table 1 for the low-energy (1.3–1.80 eV) and near-band-edge (NBE) (1.78–1.83 eV) spectral regions. Every symbol is associated to a schematic emission peak, whose width reflects that reported in literature. Additional features such as phonon replicas and overlapping peaks are also shown. The intensity is chosen arbitrarily and has no comparative meaning. The temperature dependence of the bulk CdSe band-gap (black line) [61] is also shown

Table 1　Review of CdSe PL peaks as reported in literature. Each peak is labeled with a letter and a colored symbol, by which they are referenced in the text and in Figs. 1(a) and 1(b). Column T (K) lists the temperature (in K) at which each peak was observed. In case of reports of the same peak at different T, a range is indicated, and the peak position refers to the lowest T

	Family	Label	Energy (eV)	T (K)	Assignment	Reference
Near-band-edge	Free excitons	● X_A	1.823–1.826	2–77	Free A exciton	[9, 53–57]
		X_B	1.851		Free B exciton (not shown)	[54]
	Bound excitons	■ D_1X_A	1.821–1.822	3–10	Exc. bound to donor	[53, 55, 56, 58, 59]
		■ D_2X_A	1.820	2–10	Exc. bound to donor	[54–56]
		■ A_1X_A	1.814	2	Exc. bound to acceptor	[54]
	Biexciton	★ XX	1.812	4.2	Biexciton	[58, 66]
	Other NBE	▼ D_1	1.813	5	Donor state	[56]
		▼ D_2	1.795	5	Donor state	[56]
		▼ NA_1	1.810	77	Not assigned	[58]
		▼ NA_2	1.790	4.2	Not assigned for single crystal, donor–acceptor pair (DAP) for polycrystalline	[55]
Shallow states	Peaks with phonon replica	● A	1.755	2	DAP	[54]
		● B	1.725	4.2	DAP	[55, 58]
		● C	1.784	10–70	DAP	[53]
		● D	1.709	10–70	DAP	[53]
		● E	1.732	77	DAP	[58]
	Peaks without phonon replica	■ F1–F2	1.742–1.700	3	DAP	[59]
		■ G1–G2	1.675–1.630	10–70	Impurities/defects	[53]
		■ H	1.720	77	Acceptor state or DAP	[57]
		■ I	1.690	300	Not assigned (powders)	[60]
Deep states	Bands related to TM doping	◆ J	1.50	77	Ag deep states	[58]
		◆ K	1.33	77	Cu deep states	[58]
	Other deep states	▲ L	1.550	10	Not assigned	[53]
		▲ M	1.420	10	Not assigned	[53]
		▲ N	1.400	300	Not assigned (NW sample)	[7]

Figure 1 shows that PL emission from CdSe occurs over a wide energy range. This is due to the wide range of possible intra-band-gap state energies. We group different sets of peaks according to their spectral region, since they are likely due to radiative states of similar nature [63, 64]. PL close to the band-gap is referred to as near-band-edge (NBE) emission [63], and mostly involves excitonic recombinations [63, 64]. This is the energy range covered in Fig. 1(b). At lower energies, we denote as "shallow states" peaks in the 1.60–1.78 eV range (Fig. 1(a)), and "deep states" those further into the band-gap (below 1.60 eV in Fig. 1(a)).

Low-temperature PL emission arises mainly from free excitons and excitons trapped at either neutral or charged localized sites (bound excitons) [64]. The number of photogenerated bound excitons, likewise most localized states, can saturate if the excitation power (and therefore the total number of delocalized excitons) increases [65]. Hence, their relative intensity compared to free-excitons decreases for higher power [65]. The opposite happens for biexcitonic emission [65, 66]. Since this requires interaction between two excitons, its intensity depends on n^2 (n being the density of photoexcited excitons), and therefore increases faster than that of free-excitons for increasing excitation power [65, 66]. Excitons can often be bound at donor or acceptor sites, either charged or neutral [63]. For simplicity, Table 1 and Fig. 1(b) only include NBE

emissions observed for nominally undoped CdSe. Intentional incorporation of elements such as Li, Na, P, In, or Cl [54, 58, 61, 67] may lead to several additional donor or acceptor complexes. We include in Table 1 and Fig. 1(a) "deep state" contributions arising from transition metal incorporation, since they are relevant to our investigation.

Intra-band-gap states giving optical recombinations in the "shallow states" region are commonly referred to as donor–acceptor pairs (DAP, see Table 1) [53, 55, 57–59]. However, this is quite a generic definition, as both states involved in the process (donor and acceptor) can have a number of different origins (impurities, structural defects, etc.) [63]. A way to discriminate between different DAPs is to look at their temperature dependence and note the threshold above which the emission becomes thermally quenched [68]. For example, peaks C and D in Fig. 1(a) disappear above 70 K [53], whilst peak H is seen up to 200 K (Fig. 1(b)) [57]. This can be linked to the binding energy of the shallowest state, thus providing insights on its physical nature [57].

A characteristic feature of a DAP emission is a blue-shift with excitation power [69]. In fact, the energy of a DAP transition is given by [69]

$$E_{DAP} = E_G - E_D^b - E_A^b + A e^2 / 4\pi\varepsilon\varepsilon_0 R_{DA} \qquad (1)$$

where E_G is the semiconductor band-gap, E_D^b and E_A^b are the binding energies of electron and hole to their respective (donor or acceptor) centers, and R_{DA} is the average distance between individual donors and acceptors involved in the recombination. An increased carrier population due to a higher excitation power leads to lower R_{DA}, because the average distance between occupied sites is smaller. This results in a E_{DAP} blue-shift. Peaks B, C, D, E, F1, and F2 in Fig. 1(a) were shown to follow this trend [53, 55, 58, 59]. In all cases, a blue-shift of a few meV/decade (i.e., peak energy shift when the excitation power is increased by one order of magnitude) was reported [53, 55, 58, 59].

Phonon replicas are also commonly observed in the "shallow states" spectral region [53, 55, 58]. These are radiative recombinations that involve the absorption/ emission of one or more phonons [63], and are therefore shifted by the corresponding phonon energy [63]. Accordingly, in many studies summarized in

Fig. 1(a) phonon replica appear as a series of peaks separated by a well defined energy value. This energy separation is 26.3 meV, corresponding to the longitudinal optical LO (Γ) phonon energy for CdSe [9, 70]. In a polar crystal such as CdSe, a LO phonon involves displacements of the charged atoms within the primitive cell. The macroscopic electric field generated by the relative displacements of oppositely charged atoms can interact with electrons and holes in a way similar to the piezoelectric field of acoustic phonons. This is known as Fröhlich interaction [71]. Since this depends on the phonon wave vector as q^{-1} [71], LO (Γ) phonons are predominantly involved in radiative recombination. Peaks with no phonon replica, on the other hand, often have a larger full width at half maximum (FWHM, red family in Fig. 1(a)).

The energy levels involved in "deep state" recombinations are far away from the band-edges, roughly mid-band-gap. A class of deep states particularly relevant for our work is that induced by the incorporation of transition metals [58, 72]. For example, peaks J, K in Fig. 1(a) appear as a result of Ag and Cu incorporation in CdSe [58]. At 77 K, these broad emission bands span from 1.1 to 1.8 eV, overshadowing all other contributions, including NBE emission [58]. To the best of our knowledge, there has been no study investigating the effects of Au impurities in CdSe. However, investigations of ZnSe:Ag and ZnSe:Au [72] revealed that both Ag and Au behave similarly, inducing deep states with broad emission at energies lower than NBE.

3. Experimental

CdSe nanowires are synthesized by vapor-transport in a horizontal tube, single-zone furnace [12]. Catalyst-assisted growth of CdSe NWs is carried out on Si substrates (1 cm²) coated with a thin (0.5 nm) Au layer. This de-wets prior to growth at temperatures >300 ℃, forming a distribution of isolated nanoparticles [73, 74], which initiate the nucleation and growth of CdSe nanostructures [12, 33]. As a result, dense NW forests without preferential orientation are obtained [12]. These NWs have a diameter of 29 nm ± 6 nm, as estimated by scanning electron microscopy (SEM), and they are several microns in length. After synthesis,

NWs can be mechanically transferred onto Si substrates or SiN membranes suitable for TEM. A FEI Philips XL-30 sFEG SEM and a FEI Philips Tecnai 20 TEM are used.

Catalyst-free growth is achieved using CdSe seeds (5–10 nm in diameter) produced by solution-methods [75]. These act as selective nucleation points for the vapor-transport growth of CdSe NWs [50]. These NWs are thicker than those grown with a metal catalyst, having a diameter of 170 nm ± 80 nm. We refer to this Au-free synthesis method as "seeded growth" [13, 51, 76], and label the resulting structures as seed-grown nanowires (SG-NWs), whereas the Au-catalyzed nanowires are referred to as Au-NWs. Additional structural characterization of SG-NWs and Au-NWs can be found in Figs. S-1, S-2, and S-3, in the Electronic Supplementary Materials (ESM).

Micro-PL measurements at 514.5 nm excitation are recorded on a RM1000 Renishaw system, using a 50× objective long distance (Olympus SLMPlan), which corresponds to a focused laser spot diameter of ~1.5 μm. We will refer to this as "small spot". Alternatively, the integrated PL of NW ensembles was collected using a 5× objective (Leica N-Plan, 15 μm spot diameter, large spot). In all cases, samples are placed in a He-cooled vacuum-pumped cryostat allowing optical measurements down to 10 K. The power on the sample is varied in the 0.005–10 mW range. We note that our detector efficiency drops for energies below 1.35 eV. The PL peaks are labeled following Table 1 and Fig. 1(a). Their position and width are derived from Gaussian fits.

In order to couple TEM and PL measurements on individual Au-NWs, these are transferred after growth onto separate 50-nm-thick SiN membranes. To ensure that TEM and PL are performed on the same NW, markers are patterned on the SiN membranes by electron-beam lithography prior to CdSe NWs transfer, and the CdSe NWs position is mapped via low-magnification TEM (see Fig. S-4 in the ESM). Micro-PL measurements are then performed in the cryostat, locating and probing the desired NW using the 50× objective long distance.

Laser-induced heating is a well-known issue to be considered when probing one-dimensional nanostructures [77, 78], these having a lower thermal conductivity than their bulk counterpart, and poor thermal contact with the substrate [77, 79, 80]. Laser-induced heating was observed on 7-nm-thick, undoped Si NWs for power densities higher than 10^5 W/cm^2 [77]. Here, we have thicker nanostructures (20–200 nm), and the power density is always kept lower than 10^4 W/cm^2. Above 10 K, the position of the free-exciton peak (X_A in Fig. 1(b)) is very sensitive to temperature and can be used to determine it [53]. As will be shown later, we can detect X_A shifts of 2–4 meV for temperature variations of just a few Kelvin. Since we do not see any shift by varying the excitation power at fixed temperature, we assume the temperature set by the cryostat coincides with that of the sample, even under laser irradiation.

4. Results

4.1 Au-catalyzed nanowires

Figure 2(a) shows plots of PL spectra collected at 80 K on three points of an as-grown Au-NWs sample. A representative SEM micrograph of this dense NW forest shown in the inset of Fig. 2(a). The 15 μm laser spot collects light from a large number of NWs (10^2–10^3). A broad emission band from 1.5 eV up to the NBE region (1.85 eV) can be seen, with a complex structure arising from the overlap of several radiative contributions. Some of these vary for different positions on the sample (see, e.g., the peak indicated by the arrow in the upper spectrum of Fig. 2(a)).

Figure 2(b) shows plots of PL spectra measured at 80 K on transferred wires. Given that the density of transferred NWs (Fig. 2(b), inset) is lower than in as-grown forests, the 15 μm laser spot now only probes a few tens of them. Here, emission peaks are more resolved compared to Fig. 2(a). In particular, a well-defined NBE peak is detected at 1.815 eV, consistent with the X_A emission measured for bulk CdSe at this T [9, 53, 55, 57] (Fig. 1(b)). At lower energies there is another band (labeled "O" in Fig. 2(b)), centered at ~1.7 eV. This is always found when a large spot is used to investigate the PL emission of multiple NWs, although its intensity with respect to the NBE peak may vary significantly as different sample regions are probed.
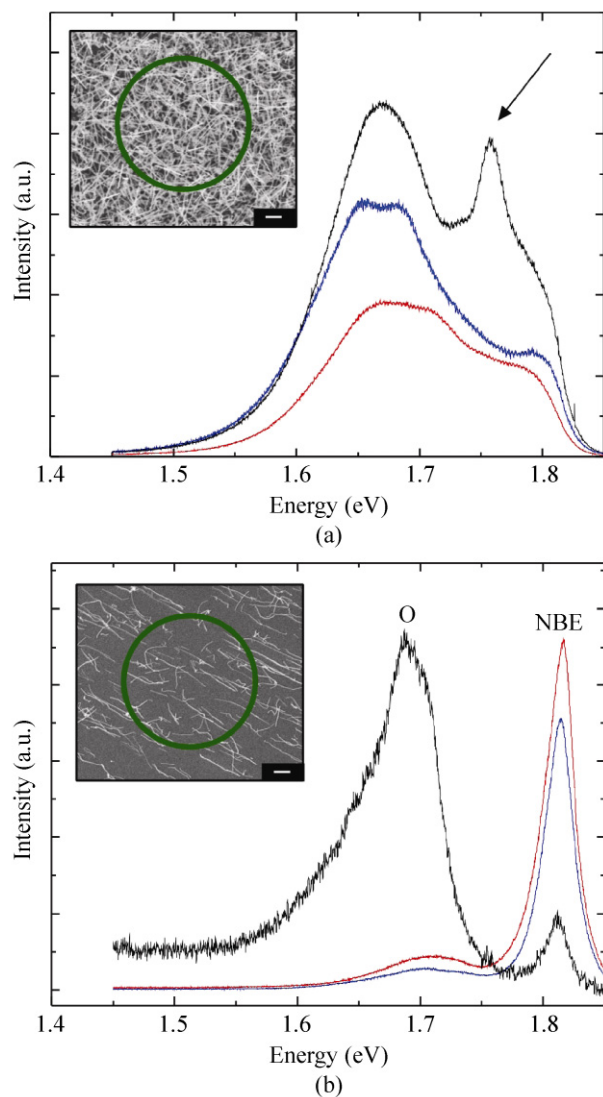
Figure 2 Large spot (15 µm) PL spectra taken at 80 K on CdSe NWs (a) as-grown on Au-coated substrates, and (b) transferred from the original substrate onto clean Si chips. Insets show representative SEM images of the illuminated areas (scale bars: 2 µm). The circles represent the laser spot sizes

To gain more insights on this band, we perform PL measurements as a function of excitation power (*P*) and temperature. Measuring a few tens of transferred wires ensures sufficient signal is collected. Figure 3(a) shows PL spectra taken at 10 K for powers varying from 10 to 0.3 mW, normalized to the O-band maximum. By increasing *P*, the relative intensity of the O-band with respect to the NBE peak drops, as is typical for recombinations from localized states [63]. Furthermore, the peak position blue-shifts ~20 meV/decade, drifting from 1.64 to 1.73 eV in Fig. 3(a). As discussed in

Section 2, this behavior is qualitatively consistent with DAP recombinations in semiconductors [69]. We note, however, that this shift is at least twice that reported for bulk CdSe (~10 meV/decade) [55, 58, 59]. An additional peak can be seen at ~1.785 eV (labeled Q in Fig. 3(a)), but is progressively overshadowed by the excitonic emission at high powers. Perna et al. [53] assigned a peak at this energy (peak C in Fig. 1(a)) to a DAP recombination. They reported a 10 meV blue-shift following a 400× increase of the excitation power, accompanied by several phonon replicas. For our samples, however, the assignment of these features is hindered by the low intensity of this contribution compared to the O band and NBE emission.

Figures 3(b) and 3(c) plot the temperature depen-dence of the O-band for fixed excitation power. In the 10–80 K range we detect a ~35 meV red-shift, more than observed for the NBE emission (~12 meV). The latter value corresponds to the temperature depen-dent shrinking of the CdSe band-gap (black curve in Fig. 1(b)) [62]. DAP recombinations are expected to exhibit this *T* response [63]. Indeed, as *T* rises, the overall PL intensity decreases, and so does the number of recombinations at the donor and acceptor sites involved in a DAP transition [6]. A reduced population of these sites would result in a larger R_{DA} in Eq. (1) shifting the emission towards lower energies, similar to Fig. 3(b). For temperatures above 100 K, the O-band intensity rapidly decreases (Fig. 3(c)). Above ~170 K, the relative intensity of the O-band with respect to NBE is no longer measurable. A similar behavior was seen for peak H in Fig. 1(a) [57], which is thermally quenched at ~200 K [57], indicating that the radiative states involved in H and O emission have similar binding energies. We never observe PL below 1.5 eV.

Figure 3 suggests that the O-band may have a DAP origin. However, if one considers the three spectra in Fig. 2(b) (taken at different points), the significant variation of O-intensity compared to the NBE implies that different NWs do not equally contribute. In order to clarify this point, we coupled small spot (1.5 µm) PL measurements to bright-field (BF) TEM imaging on isolated, individual NWs. Low-temperature PL was collected from exactly the same NWs imaged by TEM. We stress that PL from individual NWs showed no difference when measured before and after TEM
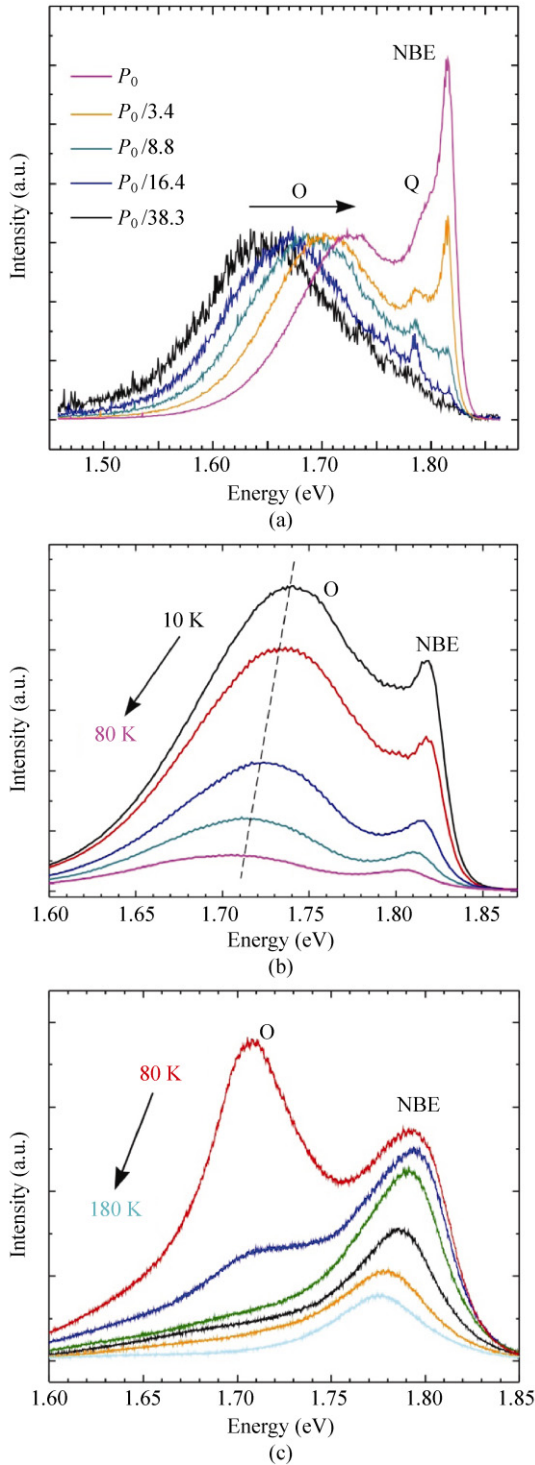
Figure 3 (a) Power and ((b), (c)) temperature dependence for large spot PL spectra taken on transferred CdSe Au-NWs. (a) Spectra measured at 10 K and normalized to the O-peak intensity. The latter is found to blue-shift when increasing the excitation power. The legend shows the beam attenuation factors for the laser power, with $P_0 = 10$ mW. (b) Data for fixed excitation power. From 10 to 80 K the O-band shows a quicker red-shift compared to NBE emission. (c) Above 100 K, the O-band becomes weaker and disappears at ~170 K

characterization, ruling out artifacts due to electron beam irradiation (see Fig. S-5 in the ESM).

Figure 4 summarizes the measured PL spectra on individual NWs, each with an associated TEM micrograph. Spectra of individual wires or small bundles can vary significantly. Whenever an isolated NW with no sign of morphological defects was measured, no O-band was seen, only NBE emission (Figs. 4(a) and 4(b)). On the other hand, the O-band appears as soon as curled bundles, or NWs with morphological defects and irregular sections, are measured (Figs. 4(c) and 4(d)). This is further supported by Fig. 4(e), showing the PL response on both edges of an individual NW several microns long. On the left side, Fig. 4(e1), this NW terminates with a curly irregular section, and the corresponding PL has a strong O contribution. As the laser spot moves towards the right side, Fig. 4(e2), where no such defects are present, the O intensity decreases. This implies that the O-band is intrinsic for our Au-NWs, but is associated to morphological defects or agglomerates.

Previous studies considered *RT* PL of individual CdSe NWs [23, 24]. However, since the O-band is quenched at *RT*, low-temperature PL is essential to correlate it with different NW morphologies. The individual NW measurements at 10 K (Figs. 4(d) and 4(e)) also allow us to resolve the separate contributions to the wide O-band seen in Figs. 2 and 3 for NW ensembles. These are centered at ~1.71 eV (O') and ~1.75 eV (O''), probably related to two defect states that give rise to DAP recombinations [53]. This common origin can be deduced from the rigid energy shift of band O with excitation power, Fig. 3(a). The lineshape only changes when band O approaches Q and NBE recombinations. The difference between O' and O'' intensities in different locations (see Fig. 4(e)) is an indication that they are related to different types (or possibly different densities) of defects. The overall O lineshape and its energy in ensemble measurements is given by the average of O' and O''.

4.2 Seeded-grown nanowires

We now compare the integrated PL emission of several SG-NWs with that of an individual wire. The density of as-grown SG-NWs can be reduced by diluting the
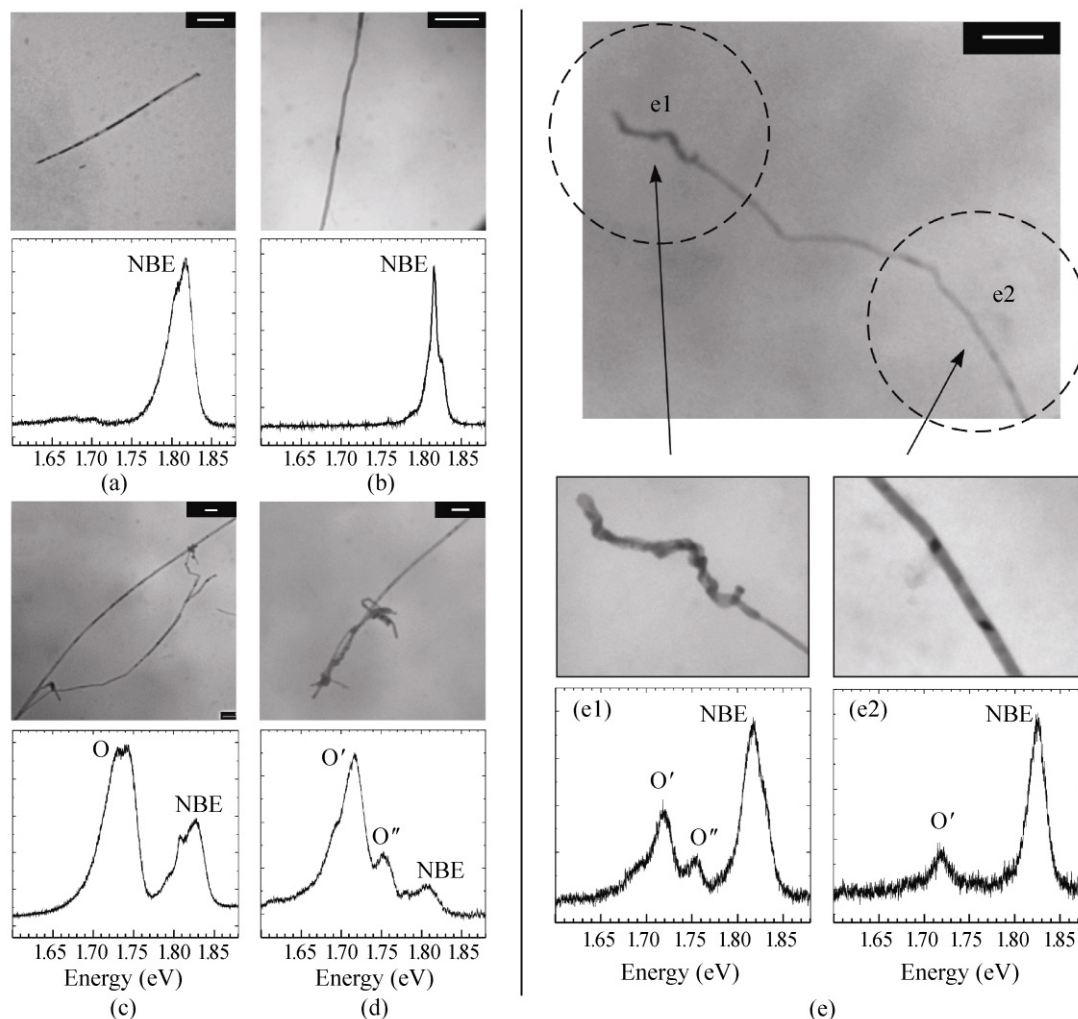
Figure 4 TEM micrographs of Au-NWs with corresponding PL spectra at T = 10 K. (a)–(d) NWs without morphological defects show no O-band emission (scale bars: 200 nm); (e) individual, partially defect CdSe Au-NW. (e1) highlights the NW section with most defects, while NBE dominates the spectrum, and low energy bands are less prominent, towards side (e2) (scale bar: 1 μm)

CdSe seed suspension [13], enabling nucleation of isolated nanostructures that can be probed directly with no need for transfer.

Figure 5(a) shows a representative PL spectrum collected at 10 K from several as-grown SG-NWs using the large laser spot (15 μm). A representative NW ensemble chosen for the measurements is shown in the inset. Figure 5(a) indicates that the NBE emission is composed of two main peaks at 1.825 and 1.821 eV. Several other peaks (at 1.765, 1.739, 1.713, and 1.687 eV) are seen at lower energies, separated by ~26 meV intervals. These can be identified as phonon replicas, as for A–E in Fig. 1(a). We label R the main zero-phonon peak at 1.765 eV.

We find similar features in the PL spectra of individual SG-NWs (Fig. 5(b)). The NBE emission is still dominated by the two peaks at 1.825 and 1.821 eV. Also, an equally intense contribution is seen at 1.773 eV with a 6 meV width, accompanied by phonon replicas (at 1.747, 1.721, and 1.694 eV), similar to Fig. 5(a). We stress that this peak is found for every SG-NW individually probed (shifted by no more than 15 meV from case to case). We thus conclude that the R peak in Figs. 5(a) and 5(b) is an intrinsic feature of crystalline SG-NWs. The larger linewidth of the R peak in Fig. 5(a) (compared to Fig. 5(b)) reflects the superposition of individual R emissions from multiple CdSe SG-NWs and the contribution from the edge of each individual SG-NW.
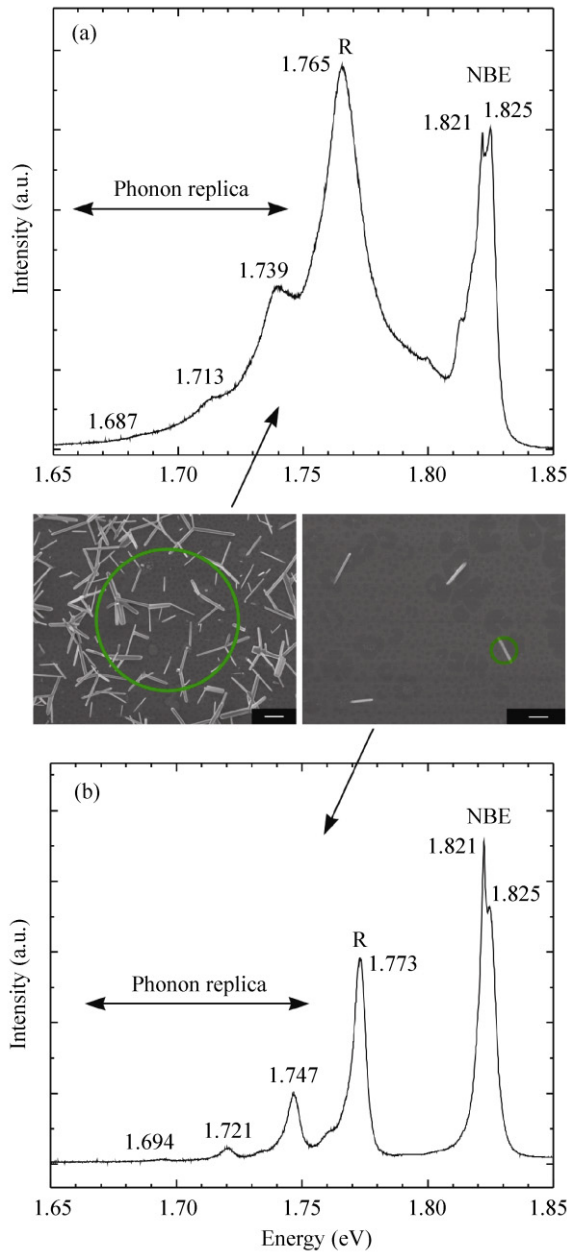
Figure 5 Comparison of PL measured at 10 K between (a) multiple and (b) single CdSe SG-NWs for large and small laser spot sizes, respectively. SEM frames show the illuminated areas (scale bars: 2 μm)

Figures 6 and 7 show plots of the power and temperature dependence of the R peak, respectively. The same trends are observed for both multiple and individual SG-NWs. Figure 6(a) shows the power dependence at 10 K, with all spectra normalized to the highest energy NBE emission peak. As the power is increased from 0.005 to 2 mW, the R/NBE intensity ratio decreases from 16 to 0.04 (Fig. 6(b)). As pointed out for the O-band above, this behavior is typical for
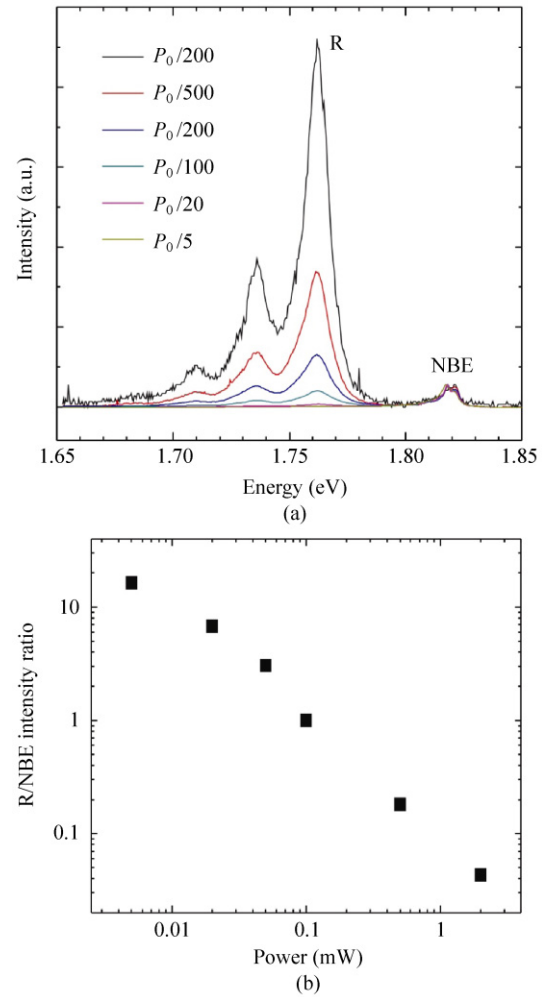

Figure 6 (a) Power dependence of SG-NWs emission at 10 K ($P_0 = 10$ mW). Spectra are normalized to the NBE intensity. (b) R/NBE intensity ratio as a function of excitation power
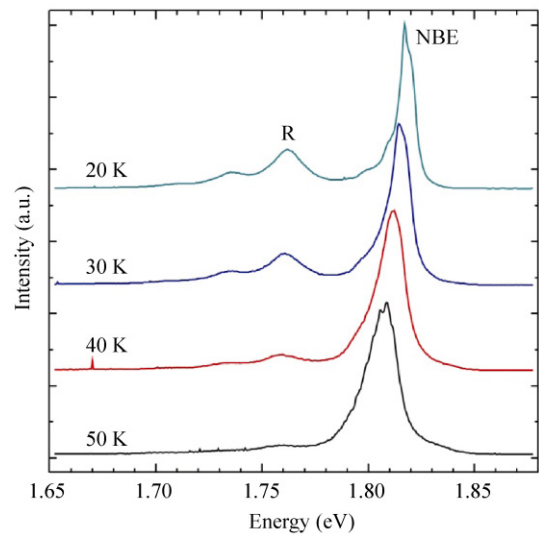

Figure 7 T dependence of SG-NW emission, showing that peak R is detectable only up to a few tens of K

recombinations occurring at localized states, which are prone to saturation as the power increases [65]. The temperature dependence in Fig. 7 shows that the R peak is hardly detectable as T rises above 50 K, similar to what has been previously reported for peaks C and D (Fig. 3(a) in Ref. [53]).

Section 2 discussed how many peaks similar to R in terms of position, phonon replicas, temperature dependence, etc. (A–E in Fig. 1(a)) were previously assigned to DAPs [53–55, 58]. We estimate the R peak shift as a function of power in Fig. 6(a) as less than 1 meV/decade. Shifts as small as 1 meV/decade were observed for DAPs [53]. The R peak is accompanied at low temperature by strong phonon replicas (here,

up to three), another indication of DAP behavior [53–55, 58]. It is thus reasonable to associate the R peak with the A–E family of DAPs (the blue peaks in Fig. 1(a)).

The power dependence of the NBE peaks for SG-NWs is reported in Fig. 8. In addition to the two peaks already observed in Fig. 5 (S at 1.825 eV and U at 1.821 eV), there is a third small peak at 1.818 eV (labeled V) seen at low powers (Fig. 8(a)). Using Table 1, we would assign peak S as the X_A exciton and U as a bound exciton, whereas V does not seem to have a match. Note that Fig. 8(a) (where spectra are normalized to peak S) and Fig. 8(b) indicate that the U intensity increases faster than S. From the
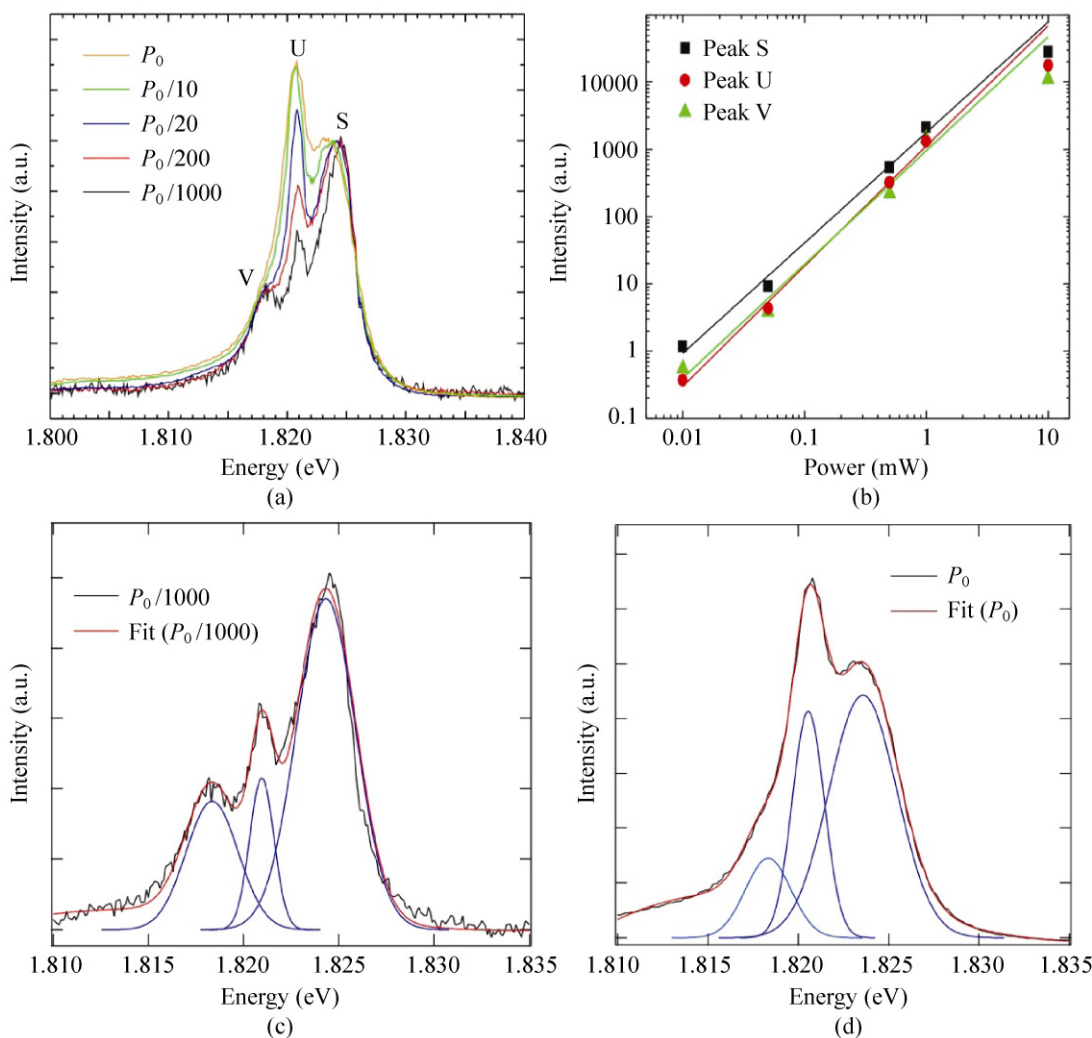

Figure 8 (a) Power dependence of NBE emission for SG-NWs at 10 K ($P_0 = 10$ mW). Spectra are normalized to the highest energy peak (S). (b) S, U, and V integrated peak intensities as a function of excitation power. (c) and (d) Fitted spectra showing the individual peak contributions for the lowest and highest excitation power, respectively

discussion in Section 2, this behavior does not follow the typical trend for bound excitons [65], being more consistent with biexcitonic emission [81, 82]. However, the spectral position of this peak does not match previous reports of biexcitons in bulk CdSe [58, 66]. Moreover, by plotting the PL intensity of S, U, and V as a function of P (Fig. 8(b)), all peaks increase superlinearly with P, as for $I_{PL} \propto P^{\alpha}$. The exponents α, evaluated neglecting the measurement at the highest power which shows saturation (Fig. 8(b)), are 1.64, 1.78, and 1.69, for S, U, V, respectively. This does not support the biexciton assignment for peak U, which would be expected to increase quadratically ($\alpha = 2$) with power [81, 82]. Hence, we assign U as a bound exciton, its position compatible with a donor-bound exciton (DX_A) [54–56], and V as an acceptor-bound exciton (AX_A) [54].

5. Discussion

5.1 Photoluminescence of individual nanowires

All spectra in Sections 4.1 and 4.2 do not show energies lower than 1.45 eV for Au-NWs and 1.65 eV for SG-NWs, since we did not detect PL beyond these limits, either from individual NWs or forests. We thus compare the low-temperature PL of individual Au-NWs and SG-NWs considering only the high-energy side of the CdSe emission spectrum (Fig. 9). The SG-NW spectrum is that of Fig. 5(b), while the Au-NW spectrum is from Fig. 4(b). In order to estimate and compare the corresponding quantum efficiencies, the spectra in Fig. 9 are measured with the same nominal parameters and normalized to the CdSe volume illuminated by the small laser spot. The volume is evaluated by measuring the length and diameter of individual nanostructures via electron microscopy. The spot diameter is used as the length when the NWs length exceeds this. Beam extinction effects are neglected.

Comparing absolute PL intensities per estimated unit volume can be prone to significant errors. However, our measurement statistics reveal that intensities for NWs grown following the same procedure at most differ by a factor of four, once normalized to the illuminated volume. In Fig. 9, the Au-NW NBE emission
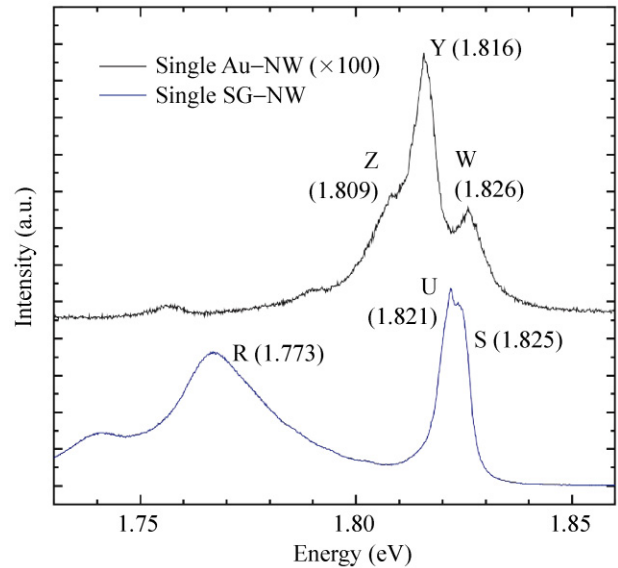

Figure 9 Comparison at 10 K between small spot PL spectra of individual Au-NWs and SG-NWs, normalized to the estimated CdSe volume under illumination. The same excitation intensity and setup is used in both cases. The Au-NW spectrum is amplified by a factor 100

is two orders of magnitude smaller than SG-NWs. This indicates that the PL efficiency per unit volume is significantly higher in SG-NWs.

The second difference in Fig. 9 is the presence of a peak~1.773 eV (labeled R) for SG-NWs. Similar peaks at ~1.751–1.754 eV are observed in some Au-NWs (O″ in Figs. 4(d) and 4(e)), while no contributions are found at similar energies for most Au-NWs. The localized donor and/or acceptor states responsible for R emission are thus not present in most Au-NWs.

Finally, we consider the shape and structure of the NBE emission. Section 4.2 showed that for SG-NWs the NBE emission is dominated by three main peaks, S (1.825 eV), U (1.821 eV), and V (1.818 eV), giving an overall NBE with FWHM ~7 meV. Conversely, for Au-NWs the three observed NBE peaks are more spread-out. The high-energy peak W (1.826 eV) is consistent with the X_A exciton. The other two peaks cannot be easily assigned on the basis of earlier reports on bulk CdSe (Table 1 and Fig. 1(b)), although it is likely that the intermediate peak (1.816 eV) could be a bound exciton [54, 55]. The third peak (1.809 eV) seems too red-shifted to be a bound exciton, and is probably due to a donor recombination [56], Fig. 1(b). Note that the overall shape of the NBE emission for Au-NWs

can change slightly from wire to wire. For example, in Fig. 4(a) the structure of the NBE complex is more difficult to resolve than in Fig. 4(b) (also in Fig. 9). On average, the combination of all NBE peaks for Au-NWs has FWHM ~30 meV, more than four times that of SG-NWs. We note as well that most previous PL investigations on single CdSe NWs were carried out at room temperature [22, 23, 26], thus preventing the observation and characterization of many of the emission features reported here.

Ideally, three major differences can be expected between the PL of a bulk sample and of a sample with reduced dimensionality (i.e., with at least one dimension comparable with the Bohr radius of CdSe, 4.9 nm [9]). First, quantum confinement in one or more dimensions can strongly alter the band-gap and related energy levels, shifting the NBE emission towards higher energies [9]. This was used to tune the emission of CdSe nanocrystals across the entire visible spectrum [83]. In addition, confinement may also occur in crystals bigger than these dimensions, but consisting of nano-crystalline domains where electrons and holes can be locally confined [24, 84]. Such domains are often the result of grain boundaries, local changes in the crystal phase, and structural disorder [24]. Second, for crystals with high surface-to-volume ratio, recombination via surface states can reduce the average carrier lifetime, and therefore the emission efficiency [85, 86]. This problem may be overcome by a suitable surface passivation, for example by embedding the nanocrystal within an epitaxial shell made of a wider band-gap semiconductor, which can confine electron–hole pairs away from the surface [85, 86]. Third, NWs PL emission can be affected by strain, which results in a shift and broadening of the PL peaks [87]. However, our large amount of statistics on single NW PL do not suggest any shift of the main NBE optical features. In particular, assuming that transferred Au-NWs would be randomly strained or bent on the TEM membrane, one would expect much more scattered peaks if the effect of strain was significant, especially in the case of highly disordered Au-NWs (Figs. 4(c) and 4(d)).

In our work, both Au-NWs and SG-NWs are not passivated, apart from the native oxide layer that forms upon exposure to atmosphere [40, 51]. Further, their surface-to-volume ratios differ by a factor of ten, owing

to the smaller diameter of Au-NWs (~30 nm) compared to SG-NWs (~200 nm). It is thus not surprising that Au-NWs have much weaker PL per unit volume (Fig. 9), as the surface influence is more pronounced. Given that PL intensity can increase up to two or three orders of magnitude upon surface passivation [85, 86], this effect may account for the difference in emission intensity between Au-NWs and SG-NWs (Fig. 9). It is also possible, however, that Au-NWs may contain a larger density of non-radiative recombination centers. Concerning quantum confinement, we note that the thinnest Au-NWs we measured have 20 nm diameter, thus still above the CdSe Bohr radius. Indeed, the position of the X_A exciton for Au-NWs (1.826 eV) is not appreciably blue-shifted with respect to the expected value for bulk CdSe at 10 K [62]. Consequently, the additional peaks seen in Fig. 9 at energies lower than the X_A exciton cannot be due to local confinement induced by structural disorder (as for Ref. [24]), and we assign them to bound excitons or donor/acceptor emission as discussed above.

Donor or acceptor states that can bind excitons and give rise to radiative transitions at energies lower than the band-gap may have different origins, which can be classified either as extrinsic impurities (incorporation of heteroatoms) or structural defects (such as, e.g., Cd or Se vacancies [88]). We also consider that: (a) Transition metals such as Au typically behave as deep acceptors in II–IV semiconductors [72]. Evidence of excitons bound at Au, Ag, or Cu acceptor sites was reported for bulk ZnTe [89], ZnSe [72], and also for ZnSe NWs [15]. In all cases, however, these were accompanied by the corresponding low-energy transition involving the deep acceptor site [16, 72, 89]. Since no low-energy contribution is found for our NWs, we do not correlate any of the NBE peaks to excitons bound to isolated Au impurities; (b) Au-NWs and SG-NWs are grown in the same furnace with the same precursors [12, 51]. Apart from Au, any other impurity should be the same (unless incorporation is strongly dependent on the growth mechanism); (c) The synthesis temperature for SG-NWs (~700 °C [51]) is higher than for Au-NWs (~450 °C [12]). This discre-pancy could not be avoided as the conditions where Au-catalysed growth occurs are not optimal for seeded-growth and vice versa [12, 51]. The higher

temperature may result in annealing of structural defects in the growing nanocrystal.

We thus conclude that SG-NWs have higher structural quality than Au-NWs. This accounts for the differences in PL emission, rather than it being due to incorporation of extrinsic impurities. It is important to note, however, that this does not necessarily imply a fundamental limitation of Au-assisted growth. It is possible that Au-catalyzed NWs grown by methods other than vapor-transport could have different PL features to those discussed here.

5.2   PL of nanowire ensembles

Many applications would benefit from NWs grown directly into devices. Hence, not only is the optical quality of individual NWs crucial, but it is also important to obtain a uniform emission from as-grown NW ensembles.

For our Au-NWs, the PL of NW ensembles differs significantly from that of individual NWs, due to the presence of several nanostructures with morphological defects, as shown in Fig. 4. Instabilities during the Au-catalyzed growth can lead to worm-like [36, 38, 90], kinked [37], twinned [30, 91], and tapered wires [12, 92]. Although we explored a wide range of parameters for the vapor-transport growth of CdSe Au-NWs and thoroughly optimized the process [12], we could not avoid having a few defected nanostructures.

In contrast to Au-NWs, our SG-NWs ensembles show essentially the same PL as a single, isolated SG-NW. In Ref. [13] we showed that SG-NWs can stem directly from individual CdSe seeds without nucleating NWs or agglomerates of low morphological quality (see

also the SEM insets in Fig. 5). Occasional branching [13] does not appreciably alter the PL emission. Therefore, even for a simple and cheap growth technique like vapor-transport, the Au-free growth can be optimized to achieve a more uniform nucleation (and therefore uniform PL) in comparison to Au-catalyzed synthesis. Further, we stress that plan-view SEM imaging can be often misleading and non-representative in evaluating the morphological quality of as-grown NWs (see, e.g., the inset in Fig. 2(a)), as a dense top-layer of straight and long wires can over-shadow a large amount of disordered wires at the bottom of the forest. The latter, though, are revealed by low-temperature PL, which is thus a powerful and non-destructive approach to evaluate the structural quality of NW ensembles.

6. Conclusions

We investigated the low-temperature PL of CdSe NWs synthesized via vapor-transport with and without a metal catalyst. A number of emission peaks (summarized in Table 2) were observed, and compared with the PL of bulk CdSe. By coupling spatially-resolved single-NW PL and TEM measurements, we separated intrinsic recombinations (seen for each individual NW) from extrinsic ones (only seen for NW ensembles or NWs with extended morphological defects). We do not ascribe the difference in optical emission between catalyst-assisted and catalyst-free NWs to Au incorporation, but rather to the different structural quality of NWs grown following different protocols. For vapor-transport growth, we find that

Table 2   Summary and proposed assignment of PL peaks observed in this work for CdSe NWs

	Peak	Energy (eV)	Best match with Table 1		Comments
Au-NW	W	1.826	X_A	(free exciton)	
	Y	1.816	------	(bound exciton)	
	Z	1.809	------	(no match)	
	Q	1.785	C	(DAP)	Extrinsic features, not seen for individual NWs
	O	1.71(O')–1.75(O")	F_1–F_2	(impurities/defects)	
SG-NW	S	1.825	X_A	(free exciton)	
	U	1.821	D_1X_A	(bound exciton)	
	V	1.818	A_1X_A	(bound exciton)	
	R	1.76–1.78	DAP		Phonon replica observed

Springer

NWs produced without a metal catalyst can be more easily optimized to yield higher PL quantum efficiency, narrower emission peaks and better uniformity over large areas, while the catalyst-assisted process is more prone to inhomogeneities.

Acknowledgements

Electronic Supplementary Material: Supplementary material (additional structural characterization of Au-NWs and SG-NWs, TEM mapping of individual Au-NWs, and a comparison of the PL emission of Au-NWs before and after electron beam exposure) is available in the online version of this article at http://dx.doi.org/ 10.1007/s12274-010-0089-2.

References

[1] Pauzauskie, P. J.; Yang, P. Nanowire photonics. *Mater. Today* **2006**, *9*, 36–45.

[2] Li, Y.; Qian, F.; Xiang, J.; Lieber, C. M. Nanowire electronic and optoelectronic devices. *Mater. Today* **2006**, *9*, 18–27.

[3] Yang, P.; Yan, R.; Fardy, M. Semiconductor nanowire: What's next? *Nano Lett*. **2010**, *10*, 1529–1536.

[4] Gur, I.; Fromer, N. A.; Chen, C. -P.; Kanaras, A. G.; Alivisatos, A. P. Hybrid solar cells with prescribed nanoscale morphologies based on hyperbranched semiconductor nanocrystals. *Nano Lett.* **2007**, *7*, 409–414.

[5] Law, M.; Greene, L. E.; Johnson, J. C.; Saykally, R.; Yang, P. Nanowire dye-sensitized solar cells. *Nat. Mater*. **2005**, *4*, 455–459.

[6] Huang, Y.; Duan, X.; Lieber, C. M. Nanowires for integrated multicolor nanophotonics. *Small* **2005**, *1*, 142–147.

[7] Shan, C. X.; Liu, Z.; Hark, S. K. Photoluminescence polarization in individual CdSe nanowires. *Phys. Rev. B* **2006**, *74*, 153402.

[8] Wang, P.; Abrusci, A.; Wong, H. M. P.; Svensson, M.; Andersson, M. R.; Greenham, N. C. Photoinduced charge transfer and efficient solar energy conversion in a blend of a red polyfluorene copolymer with CdSe nanoparticles. *Nano Lett.* **2006**, *6*, 1789–1793.

[9] Madelung, O.; Schulz, M.; Weiss, H. *Landolt–Bornstein Tables;* Springer: Berlin, 1982; Vols. 17a and 17b.

[10] Manna, L.; Scher, E. C.; Alivisatos, A. P. Synthesis of soluble and processable rod-, arrow-, teardrop-, and tetrapod-shaped CdSe nanocrystals. *J. Am. Chem. Soc.* **2000**, *122*, 12700–12706.

[11] Ma, C.; Wang, Z. L. Road map for the controlled synthesis of CdSe nanowires, nanobelts, and nanosaws—A step towards nanomanufacturing. *Adv. Mater.* **2005**, *17*, 2635–2639.

[12] Colli, A.; Fasoli, A.; Hofmann, S.; Ducati, C.; Robertson, J.; Ferrari, A. C. Deterministic shape-selective synthesis of nanowires, nanoribbons and nanosaws by steady-state vapour-transport. *Nanotechnology* **2006**, *17*, 1046–1051.

[13] Fasoli, A.; Pisana, S.; Colli, A.; Carbone, L.; Manna, L.; Ferrari, A. C. Vapor-phase nucleation of individual CdSe nanostructures from shape-engineered nanocrystal seeds. *Appl. Phys. Lett.* **2008**, *92*, 023106.

[14] Kuno, M. An overview of solution-based semiconductor nanowires: Synthesis and optical studies. *Phys. Chem. Chem. Phys.* **2008**, *10*, 620–639.

[15] Xiang, B.; Zhang, H. Z.; Li, G. H.; Yang, F. H.; Su, F. H.; Wang, R. M.; Xu, J.; Lu, G. W.; Sun, X. C.; Zhao, Q.; Yu, D. P. Green-light-emitting ZnSe nanowires fabricated via vapor phase growth. *Appl. Phys. Lett.* **2003**, *82*, 3330–3332.

[16] Zhang, X. T.; Ip, K. M.; Li, Q.; Hark, S. K. Photoluminescence of Ag-doped ZnSe nanowires synthesized by metalorganic chemical vapor deposition. *Appl. Phys. Lett.* **2005**, *86*, 203114.

[17] Zhang, B. P.; Binh, N. T.; Segawa, Y.; Kashiwaba, Y.; Haga, K. Photoluminescence study of ZnO nanorods epitaxially grown on sapphire (11$\bar{2}$0) substrates. *Appl. Phys. Lett.* **2004**, *84*, 586–588.

[18] Colli, A.; Hofmann, S.; Ferrari, A. C.; Martelli, F.; Rubini, S.; Ducati, C.; Franciosi, A.; Robertson, J. Selective growth of ZnSe and ZnCdSe nanowires by molecular beam epitaxy. *Nanotechnology* **2005**, *16*, S139–S142.

[19] Zhou, X. T.; Kim, P. S. G.; Shama, T. K.; Lee, S. T. Fabrication, morphology, structure, and photoluminescence of ZnS and CdS nanoribbons. *J. Appl. Phys.* **2005**, *98*, 024312.

[20] Wang, Z. Q.; Gong, J. F.; Duan, J. H.; Huang, H. B.; Yang, S. G.; Zhao, X. N.; Zhang, R.; Du, Y. W. Direct synthesis and characterization of CdS nanobelts. *Appl. Phys. Lett.* **2006**, *89*, 033102.

[21] Li, Q.; Brown, M. A.; Hemminger, J. C.; Penner, R. M. Luminescent polycrystalline cadmium selenide nanowires

synthesized by cyclic electrodeposition/stripping coupled with step edge decoration. *Chem. Mater.* **2006**, *18*, 3432–3441.

[22] Chèze, C.; Geelhaar, L.; Brandt, O.; Weber, W. M.; Riechert, H.; Münch, S.; Rothemund, R.; Reitzenstein, S.; Forchel, A.; Kehagias, T.; Komninou, P.; Dimitrakopulos, G. P.; Karakostas, T. Direct comparison of catalyst-free and catalyst-induced GaN nanowires. *Nano Res.* **2010**, *3*, 528–536.

[23] Venugopal, R.; Lin, P. I.; Liu, C. C.; Chen, Y. T. Surface-enhanced Raman scattering and polarized photoluminescence from catalytically grown CdSe nanobelts and sheets. *J. Am. Chem. Soc.* **2005**, *127*, 11262–11268.

[24] Protasenko, V. V.; Hull, K. L.; Kuno, M. Disorder-induced optical heterogeneity in single CdSe nanowires. *Adv. Mater.* **2005**, *17*, 2942–2949.

[25] Philipose, U.; Xu, T.; Yang, S.; Sun, P.; Ruda, H. E.; Wang, Y. Q.; Kavanagh, K. L. Enhancement of band edge luminescence in ZnSe nanowires. *J. Appl. Phys.* **2006**, *100*, 084316.

[26] Lan, A.; Giblin, J.; Protasenko, V.; Kuno, M. Excitation and photoluminescence polarization anisotropy of single CdSe nanowires. *Appl. Phys. Lett.* **2008**, *92*, 183110.

[27] Liu, Y. -H.; Wayman, V. L.; Gibbons, P. C.; Loomis, R. A.; Buhro, W. E. Origin of high photoluminescence efficiencies in CdSe quantum belts. *Nano Lett.* **2010**, *10*, 352–357.

[28] Glennon, J. J.; Tang, R.; Buhro, W. E.; Loomis, R. A.; Bussian, D. A.; Htoon, H.; Klimov V. I. Exciton localization and migration in individual CdSe quantum wires at low temperatures. *Phys. Rev. B* **2009**, *80*, 081303(R).

[29] Giblin, J.; Syed, M.; Banning, M. T.; Kuno, M.; Hartland, G. Experimental determination of single CdSe nanowire absorption cross sections through photothermal imaging, *ACS Nano* **2010**, *4*, 358–364.

[30] Agarwal, R.; Barrelet, C. J.; Lieber, C. M. Lasing in single cadmium sulfide nanowire optical cavities. *Nano Lett.* **2005**, *5*, 917–920.

[31] Borgstrom, M. T.; Zwiller, V.; Muller, E.; Imamoglu, A. Optically bright quantum dots in single nanowires. *Nano Lett.* **2005**, *5*, 1439–1443.

[32] Philipose, U.; Yang, S.; Xu, T.; Ruda, H. E. Origin of the red luminescence band in photoluminescence spectra of ZnSe nanowires. *Appl. Phys. Lett.* **2007**, *90*, 063103.

[33] Wagner R. S.; Ellis, W. C. Vapor–liquid–solid mechanism of single crystal growth. *Appl. Phys. Lett.* **1964**, *4*, 89–90.

[34] Wu, Y. Yang, P. Direct observation of Vapor–liquid–solid nanowire growth. *J. Am. Chem. Soc.* **2001**, *123*, 3165–3166.

[35] Kodambaka, S.; Tersoff, J.; Reuter, M. C.; Ross, F. M. Diameter-independent kinetics in the vapor–liquid–solid growth of Si nanowires. *Phys. Rev. Lett.* **2006**, *96,* 096105.

[36] Colli, A.; Fasoli, A.; Beecher, P.; Servati, P.; Pisana, S.; Fu, Y.; Flewitt, A. J.; Milne, W. I.; Robertson, J.; Ducati, C.; De Franceschi, S.; Hofmann, S.; Ferrari, A. C. Thermal and chemical vapor deposition of Si nanowires: Shape control, dispersion, and electrical properties. *J. Appl. Phys.* **2007**, *102*, 034302.

[37] Kamins, T. I.; Williams, R. S.; Basile, D. P.; Hesjedal, T.; Harris, J. S. Ti-catalyzed Si nanowires by chemical vapor deposition: Microscopy and growth mechanisms. *J. Appl. Phys.* **2001**, *89*, 1008–1016.

[38] Hofmann, S.; Ducati, C.; Neill, R. J.; Piscanec, S.; Ferrari, A. C.; Geng, J.; Dunin-Borkowski, R. E.; Robertson, J. Gold catalyzed growth of silicon nanowires by plasma enhanced chemical vapor deposition. *J. Appl. Phys.* **2003**, *94*, 6005–6012.

[39] Dick, K. A.; Deppert, K.; Martensson, T.; Mandl, B.; Samuelson, L.; Seifert, W. Failure of the vapor–liquid–solid mechanism in Au-assisted MOVPE growth of InAs nanowires. *Nano Lett.* **2005**, *5*, 761–764.

[40] Colli, A.; Hofmann,S.; Ferrari, A. C.; Ducati, C.; Martelli, F.; Rubini, S.; Cabrini, S.; Franciosi, A.; Robertson, J. Low-temperature synthesis of ZnSe nanowires and nanosaws by catalyst-assisted molecular-beam epitaxy. *Appl. Phys. Lett.* **2005**, *86*, 153103.

[41] Wang, Y.; Schmidt, V.; Senz, S.; Gosele, U. Epitaxial growth of silicon nanowires using an aluminium catalyst. *Nat. Nanotechnol.* **2006**, *1*, 186–189.

[42] Carlino, E. Martelli, F. Rubini, S. Franciosi, A. Catalyst incorporation in ZnSe nanowires. *Phil. Mag. Lett.* **2006**, *86*, 261–266.

[43] Allen, J. E.; Hemesath, E. R.; Perea, D. E.; Lensch-Falk, J. L.; Li, Z. Y.; Yin, F.; Gass, M. H.; Wang, P.; Bleloch, A. L.; Palmer, R. E.; Lauhon, L. J. High-resolution detection of Au catalyst atoms in Si nanowires. *Nat. Nanotechnol.* **2008**, *3*, 168–173.

[44] Oh, S. H.; van Benthem, K.; Molina, S. I.; Borisevich, A. Y.; Luo, W.; Werner, P.; Zakharov, N. D.; Kumar, D.; Pantelides, S. T.; Pennycook, S. J. Point defect configurations of supersaturated Au atoms inside Si nanowires. *Nano Lett.* **2008**, *8*, 1016–1019.

[45] Kim, B. -S.; Koo, T. W.; Lee, J. H.; Kim, D. S.; Jung, Y. C.; Hwang, S. W.; Choi, B. L.; Lee, E. K.; Kim, J. M.; Whang, D. Catalyst-free growth of single-crystal silicon and germanium nanowires. *Nano Lett.* **2009**, *9*, 864–869.

[46] Wang, N.; Tang, Y. H.; Zhang, Y. F.; Lee, C. S.; Bello, I.; Lee, S. T. Si nanowires grown from silicon oxide. *Chem. Phys. Lett.* **1999**, *299*, 237–242.

[47] Mandl, B.; Stangl, J.; Martensson, T.; Mikkelsen, A.; Eriksson, J.; Karlsson, L. S.; Bauer, G.; Samuelson, L.; Seifert, W.

Au-free epitaxial growth of InAs nanowires. *Nano Lett.* **2006**, *6*, 1817–1821.

[48] Stach, E. A.; Pauzauskie, P. J.; Kuykendall, T.; Goldberger, J.; He, R.; Yang, P. Watching GaN nanowires grow. *Nano Lett.* **2003**, *3*, 867–869.

[49] Novotny, C. J.; Yu, P. K. L. Vertically aligned, catalyst-free InP nanowires grown by metalorganic chemical vapor deposition. *Appl. Phys. Lett.* **2005**, *87*, 203111.

[50] Dai, Z. R.; Pan, Z. W.; Wang, Z. L. Novel nanostructures of functional oxides synthesized by thermal evaporation. *Adv. Funct. Mater.* **2003**, *13*, 9–24.

[51] Fasoli, A.; Colli, A.; Kudera, S.; Manna, L.; Hofmann, S.; Ducati, C.; Robertson, J.; Ferrari, A. C. Catalytic and seeded shape-selective synthesis of II–IV semiconductor nanowires. *Physica E* **2007**, *37*, 138–141.

[52] Wang, Z. L.; Kong, X. Y.; Zuo, J. M. Induced growth of asymmetric nanocantilever arrays on polar surfaces. *Phys. Rev. Lett.* **2003**, *91*, 185502.

[53] Perna, G.; Capozzi, V.; Ambrico, M. Structural properties and photoluminescence study of CdSe/Si epilayers deposited by laser ablation. *J. Appl. Phys.* **1998**, *83*, 3337–3344.

[54] Yu, P. Y.; Hermann, C. Excitation spectroscopies of impurities in CdSe. *Phys. Rev. B* **1981**, *23*, 4097–4106.

[55] Silberstein, R. P., Tomkiewicz, M. Characterization of polycrystalline electrodeposited CdSe photoelectrodes using photoluminescence spectroscopy. *J. Appl. Phys.* **1983**, *54*, 5428–5435.

[56] Arora, A. K.; Ramdas, A. K. Resonance Raman scattering from defects in CdSe. *Phys. Rev. B* **1987**, *35,* 4345–4350.

[57] Rosen, D. L.; Li, Q. X.; Alfano, R. R. Native defects in undoped semi-insulating CdSe studied by photoluminescence and absorption. *Phys. Rev. B* **1985**, *31*, 2396–2403.

[58] Kokubun, Y.; Watanabe, H.; Wada, M. Photoluminescence of CdSe single crystals. *Jap. J. Appl. Phys.* **1974**, *13*, 1393–1398.

[59] Jager-Waldau, R.; Stucheli, N.; Braun, M.; Steiner, M. L.; Bucher, E.; Tenne, R.; Flaisher, H.; Kerfin, W.; Braun, R.; Koschel, W. Thin-film CdSe: Photoluminescence and electronic measurements. *J. Appl. Phys.* **1988**, *64*, 2601–2606.

[60] Ma, C.; Ding, Y.; Moore, D.; Wang, X.; Wang, Z. L. Single-crystal CdSe nanosaws. *J. Am. Chem. Soc.* **2004**, *126*, 708–709.

[61] Henry, C. H.; Nassau, K.; Shiever, J. W. Optical studies of shallow acceptors in CdS and CdSe. *Phys. Rev. B* **1971**, *4*, 2453–2463.

[62] Tamargo, M. C. *II–IV Semiconductor Materials and their Applications;* Taylor and Francis: New York, 2002.

[63] Klingshirn, C. F. *Semiconductor Optics;* Springer: Berlin, 1997.

[64] Bogardus, E. H.; Bebb, H. B. Bound-exciton, free-exciton, band-acceptor, donor–acceptor and Auger recombination in GaAs. *Phys. Rev.* **1968**, *176*, 993–1002.

[65] Schmidt, T.; Lischka, K.; Zulehner, W. Excitation-power dependence of the near-band-edge photoluminescence of semiconductors. *Phys. Rev. B* **1992**, *45*, 8989–8994.

[66] Magde, D.; Mahr, H. Exciton–exciton interaction in CdS, CdSe, and ZnO. *Phys. Rev. Lett.* **1970**, *24*, 890–893.

[67] Tenne, R.; Jager-Waldau, R.; Lux-Steiner, M.; Bucher, E.; Rioux, J.; Levy-Clement, C. Transport and optical properties of low-resistivity CdSe. *Phys. Rev. B* **1990**, *42*, 1763–1772.

[68] Pavesi, L.; Guzzi, M. Photoluminescence of $Al_xGa_{1-x}As$ alloys. *J. Appl. Phys.* **1994**, *75*, 4779–4842.

[69] Thomas, D. G.; Gershenzon, M.; Trumbore, F. A. Pair spectra and "edge" emission in gallium phosphide. *Phys. Rev.* **1964**, *133*, A269–A279.

[70] Yu, P. Y. Resonant Raman study of LO+ acoustic phonon modes in CdSe. *Solid State Commun.* **1976**, *19*, 1087–1090.

[71] Yu, P. Y.; Cardona, M. *Fundamentals of Semiconductors;* Springer-Verlag: Berlin, 2003.

[72] Dean, P. J.; Fitzpatrick, B. J.; Bhargava, R. N. Optical properties of ZnSe doped with Ag and Au. *Phys. Rev. B* **1982**, *26*, 2016–2035.

[73] Jarrett, D. N.; Ward, L. Optical properties of discontinuous gold films. *J. Phys. D* **1976**, *9*, 1515–1527.

[74] Jiran, E.; Thompson, C. V. Capillary instabilities in thin films. *J. Elect. Mater.* **1990**, *19*, 1153–1160.

[75] Pellegrino, T.; Kudera, S.; Liedl, T.; Javier, A. M.; Manna, L.; Parak, W. J. On the development of colloidal nanoparticles towards multifunctional structures and their possible use for biological applications. *Small* **2005**, *1*, 48–63.

[76] Zhai, T.; Zhong, H.; Gu, Z.; Peng, A.; Fu, H.; Ma, Y.; Li, Y.; Yao, J. Manipulation of the morphology of ZnSe sub-micron structures using CdSe nanocrystals as the seeds. *J. Phys. Chem. C* **2007**, *111*, 2980–2986.

[77] Piscanec, S.; Cantoro, M.; Ferrari, A. C.; Zapien, J. A.; Lifshitz, Y.; Lee, S. T.; Hofmann, S.; Robertson, J. Raman spectroscopy of silicon nanowires. *Phys. Rev. B.* **2003**, *68*, 241312.

[78] Scheel, H.; Reich, S.; Ferrari, A. C.; Cantoro, M.; Colli, A.; Thomsen, C. Raman scattering on silicon nanowires: The thermal conductivity of the environment determines the optical phonon frequency. *Appl. Phys. Lett.* **2006**, *88*, 233114.

[79] Konstantinović, M. J. ; Bersier, S.; Wang, X.; Hayne, M.; Lievens, P.; Silverans, R. E.; Moshchalkov, V. V. Raman scattering in cluster-deposited nanogranular silicon films. *Phys. Rev. B* **2002**, *66*, 161311(R).

[80] Li, D.; Wu, Y.; Kim, P.; Shi, L.; Yang, P.; Majumdar, A. Thermal conductivity of individual silicon nanowires. *Appl. Phys. Lett.* **2003**, *83*, 2934–2936.

[81] Wu, Q.; Grober, R. D.; Gammon, D.; Katzer, D. S. Excitons, biexcitons, and electron–hole plasma in a narrow 2.8-nm GaAs/Al$_x$Ga$_{1-x}$As quantum well. *Phys. Rev. B* **2000**, *62*, 13022–13027.

[82] Brunner, K.; Abstreiter, G.; Böhm, G.; Tränkle, G.; Weimann, G. Sharp-line photoluminescence and two-photon absorption of zero-dimensional biexcitons in a GaAs/AlGaAs structure. *Phys. Rev. Lett.* **1994***, 73*, 1138–1141.

[83] Bruchez, M. Jr.; Moronne, M.; Gin, P.; Weiss, S.; Alivisatos, A. P. Semiconductor nanocrystals as fluorescent biological labels. *Science* **1998**, *281*, 2013–2016.

[84] Intonti, F.; Emiliani, V.; Lienau, C.; Elsaesser, T.; Notzel, R.; Ploog, K. H. Low temperature near-field luminescence studies of localized and delocalized excitons in quantum wires. *J. Microsc.* **2001**, *202*, 193–201.

[85] Han, X.; Kou, L.; Lang, X.; Xia, J.; Wang, N.; Qin, R.; Lu, J.; Xu, J.; Liao, Z.; Zhang, X.; Shan, X.; Song, X.; Gao, J.; Guo, W.; Yu, D. Electronic and mechanical coupling in bent ZnO nanowires. *Adv. Mater.* **2009**, *21*, 4937–4941.

[86] Sköld, N.; Karlsson, L. S.; Larsson, M. W.; Pistol, M. -E.; Seifert, W.; Trägårdh, J.; Samuelson, L. Growth and optical properties of strained GaAs–Ga$_x$In$_{1-x}$P core–shell nanowires. *Nano Lett.* **2005**, *5*, 1943–1947.

[87] Jabeen, F.; Rubini, S.; Grillo, V.; Felisari, L.; Martelli, F. Room temperature luminescent InGaAs/GaAs core–shell nanowires. *Appl. Phys. Lett.* **2008**, *93*, 083117.

[88] Kobayashi, A.; Sankey, O. F.; Dow, J. D. Deep energy levels of defects in the wurtzite semiconductors AlN, CdS, CdSe, ZnS, and ZnO. *Phys. Rev. B* **1983**, *28*, 946–956.

[89] Venghaus, H.; Dean, P. J. Shallow-acceptor, donor, free-exciton, and bound-exciton states in high-purity zinc telluride. *Phys. Rev. B* **1980**, *21*, 1596–1609.

[90] Kikkawa, J.; Ohno, Y.; Takeda, S. Growth rate of silicon nanowires. *Appl. Phys. Lett.* **2006**, *86*, 123109.

[91] Johansson, J.; Karlsson, L. S.; Svensson, C. P. T.; Martensson, T.; Wacaser, B. A.; Deppert, K.; Samuelson, L.; Seifert, W. Structural properties of <111>B-oriented Ⅲ–Ⅴ nanowires. *Nat. Mater.* **2006**, *5*, 574–580.

[92] Hannon, J. B.; Kodambaka, S.; Ross, F. M.; Tromp, R. M. The influence of the surface migration of gold on the growth of silicon nanowires. *Nature* **2006**, *440*, 69–71.